On coherent structures and mixing characteristics in the near field of a rotating-pipe jet

Mullyadzhanov, R; Abdurakipov, S.S.; Hanjalic, K.

DOI
10.1016/j.ijheatfluidflow.2016.06.018

Publication date
2017

Document Version
Final published version

Published in
International Journal of Heat and Fluid Flow

International Journal of Heat and Fluid Flow 63 (2017) 139–148

Contents lists available at ScienceDirect

International Journal of Heat and Fluid Flow

journal homepage: www.elsevier.com/locate/ijhff

On coherent structures and mixing characteristics in the near field of a rotating-pipe jet

R. Mullyadzhanov[a,b,*], S. Abdurakipov[a,b], K. Hanjalić[b,c]

[a] Institute of Thermophysics SB RAS, Lavrentyeva 1, Novosibirsk 630090, Russia
[b] Novosibirsk State University, Pirogova 2, Novosibirsk 630090, Russia
[c] Delft University of Technology, ChemE Dept., Julianalaan 136, 2628 BL Delft, The Netherlands

ARTICLE INFO

Article history:
Available online 26 July 2016

Keywords:
Swirling jets
Mixing
Coherent structures

ABSTRACT

Mixing characteristics and coherent structures populating the near-nozzle area of a rotating-pipe jet at the Reynolds number of 5300 were studied by Large-eddy simulation (LES). The swirl rate, defined as the ratio of the tangential velocity of the inner pipe wall to the bulk axial velocity, varied from 0 to 1, corresponding to a weak-to-moderate swirl intensity, insufficient to induce reverse flow near the nozzle. The visualization shows that for the non-swirling jet the near-wall streaky structures generated in the pipe interact with the shear layer, evolving into hairpin-like structures that become tilted at low rotation rates. For higher swirl, they cannot be recognized as they are destroyed at the nozzle exit. No large-scale coherent structures akin to Kelvin–Helmholtz vortical rings in the 'top-hat' jets are identifiable close to the nozzle. Using the single and joint probability density functions of velocity and passive scalar (temperature) fields we quantify the events responsible for the intensive entrainment at various swirl numbers. The isosurface of the temperature field indicates the meandering and precessing motion of the rotating jet core at the axial distance of 6D downstream, where D is the diameter of the pipe. The Fourier analysis with respect to the azimuthal angle and time reveals an interplay between the co- and counter-rotating modes. These findings explain the previously detected but not fully clarified phenomenon of the weakly counter-rotating jet core at low swirl rates.

1. Introduction

Swirling flows have long been in the research focus because of their versatile industrial application for promoting mixing, phase separation, flame stabilization and control, but also because of their interesting flow physics. Among the variety of configurations, the free swirling jets have a kind of canonical significance as they contain most generic features of swirling flows, but are void from the effects of confinement and solid walls. The rotation-generated pressure gradient that dominates the jet near-field at strong swirl rates with a consequent vortex breakdown and flow recirculation, and enhanced mixing and entrainment of surrounding fluid imparted by the swirl-induced shear, are the main features that distinguish the swirling jets from their non-swirling surrogate.

A round jet is usually generated by forcing fluid through a smooth-contraction nozzle generating a close-to-laminar 'top-hat' velocity profile (Ball et al., 2012). However, it is well known that the nozzle shape and geometry as well as the upstream conditions determine the characteristics of the jet through the level of turbulence and the momentum thickness of the boundary layer at the nozzle walls. Moreover, the nozzle with a contraction produces an undesired overshoot at the centre of the axial velocity profile when a moderate level of rotation is applied to the flow inside the swirl-generating device (Alekseenko et al., 2008; Billant et al., 1998; Leclaire and Jacquin, 2012; Oljaca et al., 1998; Panda and McLaughlin, 1994). Thus, in order to analyze possible flow regimes one needs to vary a wide range of parameters. Inevitably, issues arise when the results are compared with those obtained by other researchers using different swirling facilities. A reliable and comprehensive data-set on a well-defined canonized swirling jet is thus much desired to serve as a reference for benchmarking other numerical and experimental studies on swirling flows.

When considering a canonical jet, one tries to reduce the number of dimensionless parameters governing the flow. To eliminate the effects of nozzle geometry, a plausible option is to study the jet issuing from a round pipe. If the pipe is long enough, the flow at the exit corresponds to the fully developed turbulent regime where only one parameter, i.e., the Reynolds number, determines the flow.

* Corresponding author.
E-mail address: rustammul@gmail.com (R. Mullyadzhanov).

http://dx.doi.org/10.1016/j.ijheatfluidflow.2016.06.018
0142-727X/

In case of swirling flows, a long pipe rotating around its axis represents a canonical swirling jet with a unique inflow velocity profile unlike various swirling devices (Örlü, 2009). In the present work with the use of Large-eddy simulations (LES) we focus on the rotating pipe jet at low-to-moderate swirl. The inflow conditions are provided with a separate periodic pipe flow simulations mimicking very long supplying duct. The Reynolds number, Re, based on the bulk velocity U_b and pipe diameter D, is 5300 and swirl number $N = U_w/U_b$ varies from 0 to 1, where U_w is the tangential velocity of the pipe rotating around its axis.

One of the first experiments on a rotating pipe jet was performed by Rose (1962). He described the bulk effect of swirl such as the increase of the spreading and entrainment rates together with the higher level of turbulence and faster decay of the axial velocity compared to the non-rotating jet. Pratte and Keffer (1972) confirmed conclusions of Rose and examined the streamwise variation of the mean axial and tangential velocity showing x^{-1} and x^{-2} dependence, respectively, where x is the streamwise coordinate, which is in agreement with the theoretical considerations by Loitsianskii (1953), Mullyadzhanov and Yavorskii (2013), among others. Mehta et al. (1991) quantified the changes in the Reynolds stresses with the increase in N up to 0.4. Facciolo and Alfredsson (2004) studied a swirling pipe jet at Re up to 33,500 and $N = 0.5$. The experimental facility featured a long enough pipe of $100D$ to provide a fully developed turbulent conditions at the nozzle exit. They studied the near-field time-averaged turbulent characteristics and observed the phenomenon of the weak jet core counter-rotation around $x = 6D$ attributing it to the effect of the Reynolds stresses on the mean field. Further experimental and numerical observations are described by Facciolo et al. (2007) focusing on both, the rotating pipe and jet flows. Örlü and Alfredsson (2008) used the same setup to perform simultaneous velocity and passive scalar point measurements of a slightly heated swirling air pipe jet at $Re = 24,000$ and $N = 0.5$ together with a non-swirling counterpart. They observed high intermittency of both fields and calculated joint probability density distributions of velocity components and temperature. Maciel et al. (2008) using LES and experimental data discussed the phenomenon of counter-rotating core and proposed an explanation in terms of the angular momentum transport.

A swirling quasi-laminar flow issuing from a relatively short pipe has been investigated experimentally by Liang and Maxworthy (2005) at $Re = 1000$. The authors studied the flow at different rotation rates observing various azimuthal instabilities in the form of helical waves at moderate swirl numbers. Particular attention has been paid to the global instability mode as a result of the vortex breakdown regime with reverse flow region near the nozzle at high rotation rates causing large-scale fluctuations in the form of a spiral vortex. The vortex breakdown phenomenon attracted a lot of attention in the literature and is well reviewed by Lucca-Negro and O'Doherty (2001) among others. Using LES Luginsland and Kleiser (2015), Luginsland (2015) and Luginsland et al. (2016) studied the laminar inflow pipe jet with solid-body rotation and $N \approx 1.3$ featuring reverse flow near the pipe exit. They observed high sensitivity of the position and size of the vortex breakdown bubble to boundary conditions, thickness of the pipe wall and inflow perturbations. Sanmiguel-Rojas et al. (2008) investigated numerically the laminar flow discharging from a rotating pipe into a cylindrical container through a 1: 8 sudden expansion. They showed a transition map for various flow regimes in the $Re - N$ plane, analyzed helical perturbations generated in the rotating pipe and their effect on the jet flow and vortex breakdown phenomenon. Recently Miranda-Barea et al. (2015) performed experiments confirming the results of Sanmiguel-Rojas et al.

The paper is organized as follows. Section 2 describes the computational details and flow configuration. In Section 3 we describe the time-averaged characteristics of the flow. The dynamical features are analyzed in Section 4 followed by conclusions.

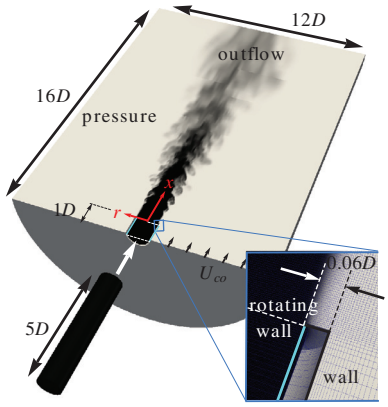

Fig. 1. Half of the computational domain, cylindrical coordinate system (r, ϕ, x) and boundary conditions. The instantaneous field is visualized by the temperature. The $5D$ pipe is used to simulate the unsteady inflow conditions with a periodic boundary conditions.

2. Governing equations and computational details

The LES is performed with the TU Delft unstructured finite-volume computational code T-FlowS (Ničeno and Hanjalić, 2005). The diffusion and convection terms are discretised by the second-order central-difference scheme, whereas the time-marching is performed using a fully-implicit three-level time scheme. We solve the non-dimensional spatially filtered transport equations for mass, momentum and passive scalar (temperature) to determine the dynamics and mixing of the incompressible fluid:

$$\frac{\partial U_i}{\partial x_i} = 0,$$
$$\frac{\partial U_i}{\partial t} + \frac{\partial U_i U_j}{\partial x_j} = -\frac{\partial P}{\partial x_i} + \frac{1}{Re}\frac{\partial^2 U_i}{\partial x_j^2} - \frac{\partial \tau_{ij}}{\partial x_j},$$
$$\frac{\partial T}{\partial t} + \frac{\partial T U_j}{\partial x_j} = \frac{1}{PrRe}\frac{\partial^2 T}{\partial x_j^2} - \frac{\partial q_j}{\partial x_j},$$

where U_i and T are the resolved velocity vector and temperature. We assume the working fluid to be air with the Prandtl number, $Pr = \nu/\alpha = 0.71$, where ν is the kinematic viscosity of the fluid and α its thermal diffusivity. The stress tensor τ_{ij} represents the influence of the subgrid scales on resolved motion and is modelled using the dynamic Smagorinsky model as follows, $\tau_{ij} = -2\nu_t S_{ij} + \tau_{kk}\delta_{ij}/3$, where S_{ij} is the strain-rate tensor, δ_{ij} the Kronecker delta and $\nu_t = (C_s\Delta)^2\sqrt{2S_{ij}S_{ij}}$ the turbulent viscosity. The Smagorinsky constant C_s is determined dynamically according to the standard routine (Germano et al., 1991); Δ is the local grid size. The subgrid-scales heat flux term is defined in a similar manner, $q_j = (\nu_t/Pr_t)(\partial T/\partial x_j)$, where the turbulent Prandtl number is assumed constant, $Pr_t = 0.9$.

We consider a fully turbulent canonical rotating-pipe jet configuration. The computational domain was in the form of a cylinder of $12D$ in diameter and $16D$ in length, Fig. 1. A precursor simulation of the fully developed $5D$-long rotating pipe flow generated the inflow conditions for each N considered (see Appendix A). A stored time series of the precursor unsteady velocity field was then imposed as the inflow conditions at the $r - \phi$ cross-section at the inlet ($x = -1D$) of a $1D$-long pipe segment immersed into the computational domain, Fig. 2. The incoming flow with $Re = 5300$ and N varying from 0 to 1 with a step of 0.25 had a normalized temperature $T = 1$. A small co-flow of $U_{co} = 0.04U_b$ with $T = 0$ was

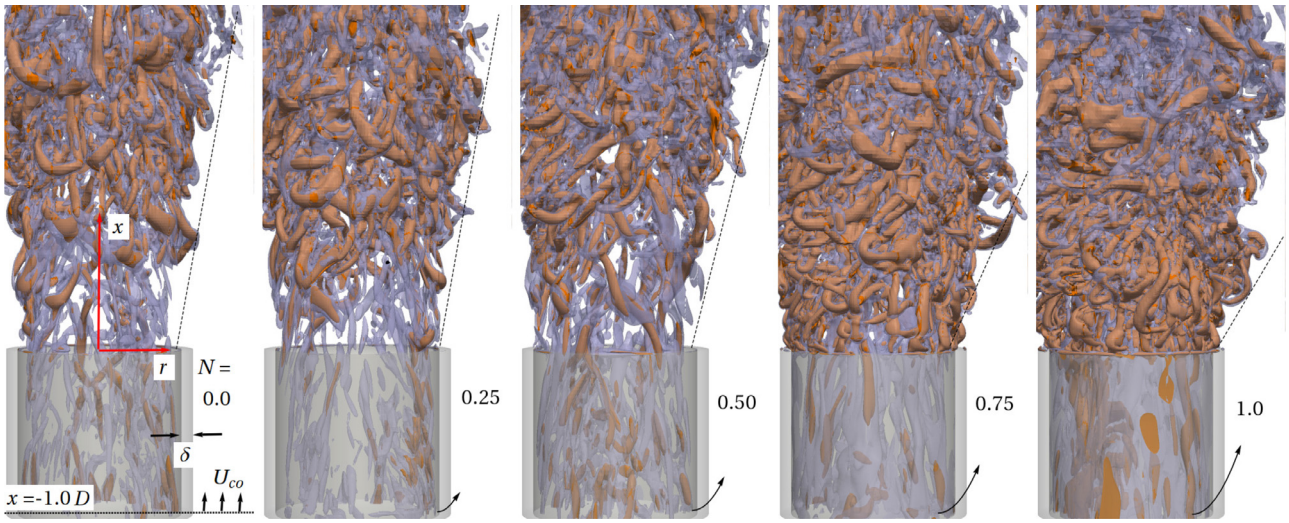

Fig. 2. Visualization of vortical structures near the nozzle of the jet using two isosurfaces of the Q-criterium with $Q = 0.5$ (transparent violet) and $Q = 1.5$ (orange) for various rotation rates N ranging from 0 to 1. Black arrows show the clockwise rotation direction of the inner wall of the pipe. Dashed line schematically shows the spreading rate of the jet. (For interpretation of the references to colour in this figure legend, the reader is referred to the web version of this article.)

imposed at the inlet of the pipe-surrounding domain at $x = -1D$. The pipe wall thickness was $\delta = 0.06D$ with only inner side rotating. Walls were assumed to be adiabatic. The convective outflow was set at the exit boundary, while constant pressure was imposed on the open lateral boundary. The LES grid had a DNS-like resolution in the near-nozzle area and consists of 252 × 282 × 264 cells (∼ 16.7 × 10^6) in the radial, axial, and azimuthal directions, respectively, with the majority clustered in shear layers and near-wall regions with the stretching factor being less than 5% . The minimum axial spacing $\Delta x = 0.005D$ was at the nozzle exit, where the ratio of the local grid size to Kolmogorov scale was around 1.0. The ratio of the time-averaged eddy viscosity to the molecular one, $\overline{\nu}_t/\nu$, was below 1.0 in most of the domain reaching the value of 2.0 in shear layers at $x/D \approx 8$. The computational time step was $\Delta t = 2.5 \times 10^{-3} D/U_b$. All simulations run for at least 150 non-dimensional time units to avoid the effect of transients corresponding to approximately 10 flow-through times and another 150 time units to collect statistics. The simulation with the rotation number N were initialized from the previous fully developed jet flow with lower N. The results presented below were non-dimensionalized with U_b and $\Delta T = 1$ (the temperature difference between the inflow and co-flow).

Figure 2 shows typical vortices in the near field of the jet visualized by constant levels of the Q-criterium where $Q = (\Omega_{ij}\Omega_{ij} - S_{ij}S_{ij})/2$ with Ω_{ij} and S_{ij} being the rotation rate and the rate-of-strain tensors, respectively. In contrast to 'top-hat' jets with Kelvin–Helmholtz vortex rings as the dominant structures (Ball et al., 2012), the pipe flow supplies streamwise streaks which can be traced in the range of $0 \le x/D \le 1$. For $N = 0$ the interaction of streaky structures and the shear layer of the jet leads to the formation of large-scale hairpin-like structures at $x/D > 0.5$. As in the weakly swirling 'top-hat' jets where the rotation leads to tilted vortex rings (McIlwain and Pollard, 2002), in case of the pipe jet the observed hairpins are also slightly inclined for low rotations, $N = 0.25$. However, for higher swirl they can hardly be recognized. For relatively high rotation rates ($N \ge 0.75$) the structures existing in the pipe are immediately destroyed by a strong azimuthal shear layer in the vicinity of the nozzle edge.

Fig. 3 shows the time-averaged axial ($\overline{U}_x$) and tangential ($\overline{U}_\theta$) velocity profiles inside the pipe at $x = -1D$ for various N. The increase in swirl leads to a well-known relaminarizing effect with

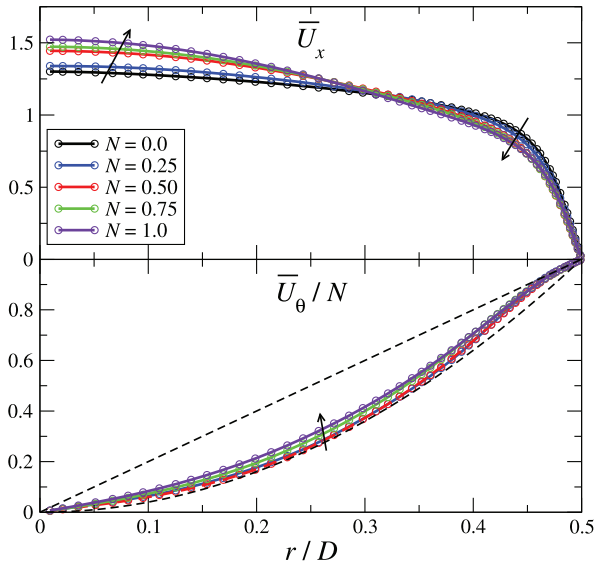

Fig. 3. Radial time-averaged axial and azimuthal velocity profiles at $x = -1.0D$ inside the pipe. Arrows indicate the increase in swirl. Dashed lines correspond to the linear function and parabola.

the axial velocity increasing in the center of the pipe. The profile of $\overline{U}_\theta$ approaches a parabola due to the influence of turbulent stresses while laminar rotating pipe flow demonstrates a solid-body rotation distribution (Orlandi and Fatica, 1997). At the range of rotation rates considered in the present study, the Reynolds stresses do not vary significantly with N (see Appendix A). To compare results with other studies, we calculate the swirl number based on definitions in the literature:

$$S_1 = \frac{\int \overline{U}_x \overline{U}_\theta r^2 dr}{D/2 \int \overline{U}_x^2 r dr},$$

$$S_2 = \frac{\int \overline{U}_x \overline{U}_\theta r^2 dr}{D/2 \int \left(\overline{U}_x^2 - \overline{U}_\theta^2/2\right) r dr}.$$

Table 1
The swirl number values according to various definitions.

N	S_1	S_1^{lam}	S_2	S_2^{lam}
0	0	0	0	0
0.25	0.076	0.096	0.077	0.098
0.50	0.142	0.182	0.148	0.193
0.75	0.220	0.271	0.243	0.310
1.0	0.296	0.360	0.358	0.462

Table 1 summarizes values of the swirl number according to different definitions. The maximum value $S_2 \approx 0.36$ corresponds to $N = 1$. Note that S^{lam} in the table is calculated for a given axial velocity profile as in Fig. 3 assuming solid-body rotation, $\overline{U}_\theta(r) = 2Nr/D$. All cases correspond to low-swirl jets without reverse flow. As mentioned in the introduction, Luginsland and Kleiser (2015), Luginsland (2015) and Luginsland et al. (2016) studied a similar pipe jet configuration with $N \approx 1.3$ with the inflow set by analytic velocity profiles. Their case featured the vortex breakdown because of the high $S_2 = S_2^{lam} \approx 0.8$ due to the solid-body-rotation profile of the tangential velocity at the inflow.

3. Mean characteristics

With the increase in N the flow field significantly changes. Fig. 4 shows the decay of the centreline $\overline{U}_x$, maximum of $\overline{U}_\theta$ at the given x and centreline rms of u_x, rms of u_r, $\overline{T}$ and rms of θ with the distance downstream, where u and θ are the velocity and temperature fluctuations. LES results for the mean axial velocity are validated against the direct numerical simulations by Sandberg et al. (2012) at close Reynolds number but with a much higher co-flow, as well as with PIV experiments of a non-swirling pipe jet at $Re = 6000$ by Capone et al. (2013). The axial momentum rapidly decays when the rotation is applied to the flow. Apart from faster spreading rate of the jet, the swirl significantly modifies the flow in the pipe making the shear layer of the jet thicker (see Fig. 3) leading to rapid diffusion of the axial velocity. The axial decay of the mean tangential velocity peak is shown in Fig. 4(b). The agreement with the data of Örlü and Alfredsson (2008) is very good for $N = 0.5$ even though the experiment was performed at $Re = 24,000$. Note that the azimuthal velocity decreases exponentially and already at $x/D = 10$ the level of swirl is negligible compared to the axial velocity. The velocity fluctuations show excellent agreement with the data of Sandberg et al. (2012). While u_r agrees well with the data of Capone et al. (2013), u_x has a higher level in experiments indicating that the pipe flow was not fully developed. The temperature along the centreline decays with the same rate as the axial velocity. The higher the value of N, the faster is the decrease of $\overline{T}$. The agreement with $\overline{T}$ and θ measurements of Örlü and Alfredsson (2008) at $N = 0.5$ is also very good although the experiments show some scatter of the data at $x/D = 3$ and 4.

Fig. 5 shows the radial profiles of $\overline{U}_x$ and $\overline{U}_\theta/N$ at different axial positions. While at $x/D = 1$ for low swirl the axial velocity profile of a fully developed pipe flow can be identified, for higher N it has a Gaussian shape even close to the nozzle. For further stations and higher swirl the axial velocity decays and diffuses faster according to previous observations. Tangential velocity profile normalized with N can still be described as a parabola in the central part. The peak value of $\overline{U}_\theta$ decreases rapidly with x according to Fig. 4. At the latest considered here station $x/D = 6$ a relatively small area of negative $\overline{U}_\theta$ appears in the jet core for high rotation rates. It occurs already at $N = 0.5$ at the axial distance of $x/D = 5.5 - 5.8$ with the width of $r/D \approx 0.14$. At higher rotation rates this phenomenon is more pronounced. For $N = 0.75$ the negative region of $\overline{U}_\theta$ spans from $x/D = 5.5$ to 6.4 with maximum width of $r/D \approx 0.17$.

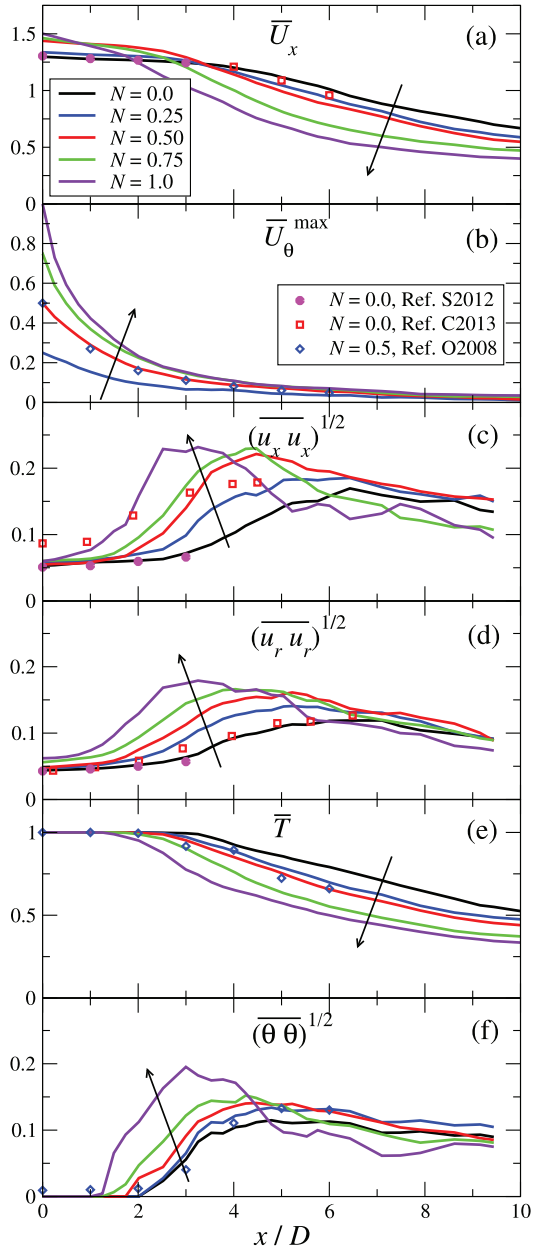

Fig. 4. (a): Time-averaged axial velocity along the centreline, (b): maximum of the mean tangential velocity at the given axial position, (c): axial velocity fluctuations along the centreline, (d): radial velocity fluctuations, (e): the time-averaged temperature and (f): temperature fluctuations for various N. The data from the literature is shown by symbols (S2012: Sandberg et al. (2012), C2013: Capone et al. (2013), O2008: Örlü and Alfredsson (2008)). Arrows indicate the increase in swirl.

For the highest swirl, $N = 1.0$, $\overline{U}_\theta < 0$ is first observed at $x/D \approx 4.5$ ending at 6.2. At this rotation rate the maximum value of negative $\overline{U}_\theta$ is around 2% of U_b with the maximum $\overline{U}_\theta < 0$ region width of $r/D \approx 0.22$. As mentioned in the Introduction this phenomenon of the counter-rotating jet core has been first observed in the experiments of Facciolo and Alfredsson (2004). Further observations were done by Facciolo et al. (2007); Örlü and Alfredsson (2008) and Maciel et al. (2008). Although the latter work included LES results and as a consequence the instantaneous volumetric data, the research was mainly focused on the time-averaged analysis, i.e., the description of Reynolds stresses. In the next section we provide information on dynamical features seeking the explanation for this unresolved phenomenon.

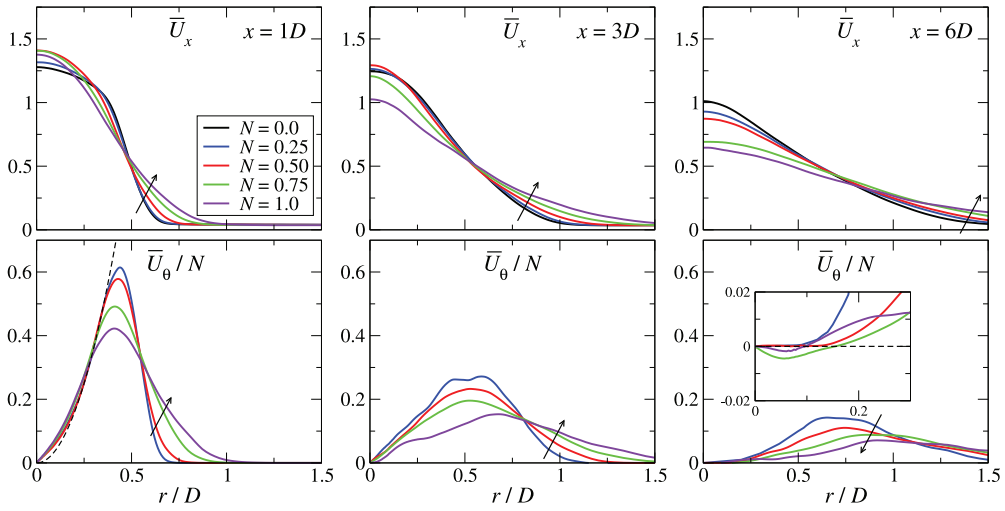

Fig. 5. Radial time-averaged axial and tangential velocity profiles at $x/D = 1$, 3 and 6 for various N. The profiles of $\overline{U}_\theta$ are normalized with N. Arrows indicate the increase in swirl. The dashed line in the left bottom figure corresponds to parabola. The inset in the right bottom figure shows the small area of the negative mean tangential velocity corresponding to the phenomenon of the counter-rotating jet core.

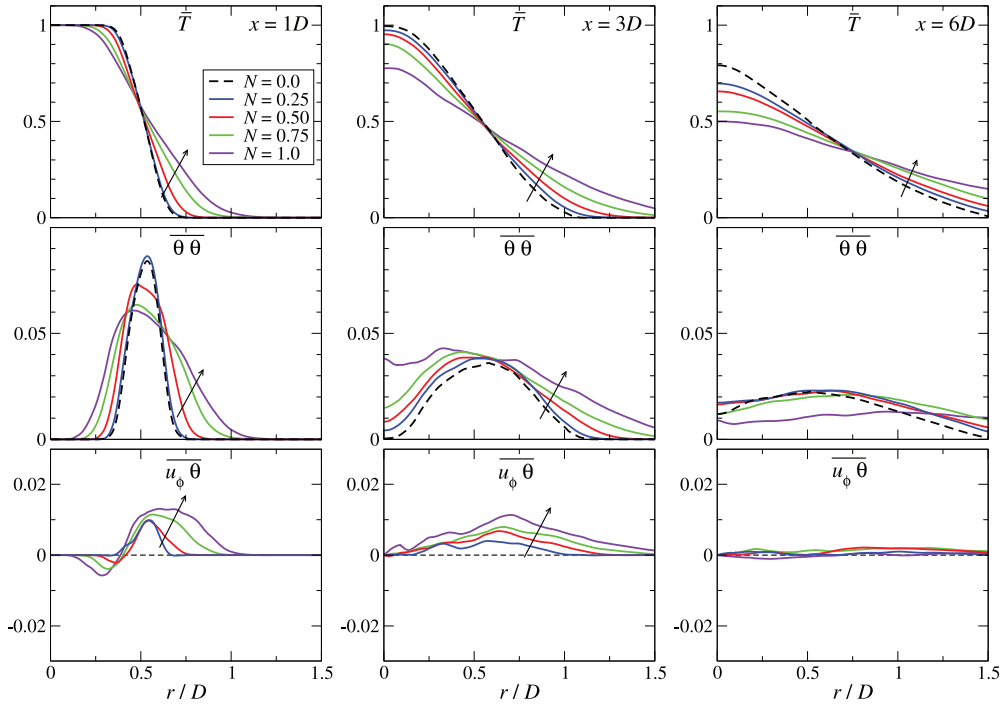

Fig. 6. Radial time-averaged profiles of $\overline{T}$, its fluctuations and velocity-temperature correlations at $x/D = 1$, 3 and 6 for various N. Arrows indicate the increase in swirl.

The normal components of the Reynolds stresses tensor monotonically increase with N up to $x/D = 4$ (see Fig. 4). At the same time at $x/D = 6$ the fluctuations appear to be the weakest for $N = 1.0$ due to the rapid decrease of the axial velocity. Fig. 6 shows the radial profiles of $\overline{T}$, $\overline{\theta\,\theta}$ and $\overline{u_\phi\theta}$. As mentioned above, $\overline{T}$ generally follows the trend of the axial velocity. Thus, the higher the rotation rate, the faster diffusion is for the temperature profile. Contrary to the normal components of the Reynolds stresses, $\overline{\theta\,\theta}$ does not monotonically grow with N close to the nozzle. At $x/D = 1$ the peak is the highest for $N = 0.0 - 0.25$ while the profile of $\overline{\theta\,\theta}$ is much wider for $N = 1.0$. The components $\overline{u_x\theta}$ and $\overline{u_r\theta}$ (not shown here) remain positive for all N while the radial profile of $\overline{u_\phi\theta}$ changes the sign at $r/D \approx 0.5$ having a negative peak close to the center for high rotation rates. This behaviour of $\overline{u_\phi\theta}$ is similar to $\overline{u_\phi u_r}$ and $\overline{u_x u_\phi}$ shear components of the Reynolds stresses (not shown here) while $\overline{u_x u_r}$ is also positive for all N. In the next Section we investigate this further with the use of instantaneous velocity and temperature fields as well as the single and joint probability density distributions to understand the interaction of velocity-velocity and velocity-temperature fluctuations close to the nozzle.

4. Dynamical flow features

Fig. 7 gives the impression on the entrainment process showing axial velocity and temperature fields at $x/D = 0.5$ together with streamlines in the $r - \phi$ plane. While at $N = 0.0 - 0.25$ the turbulence resembles closely the familiar stagnant-pipe near-wall flow

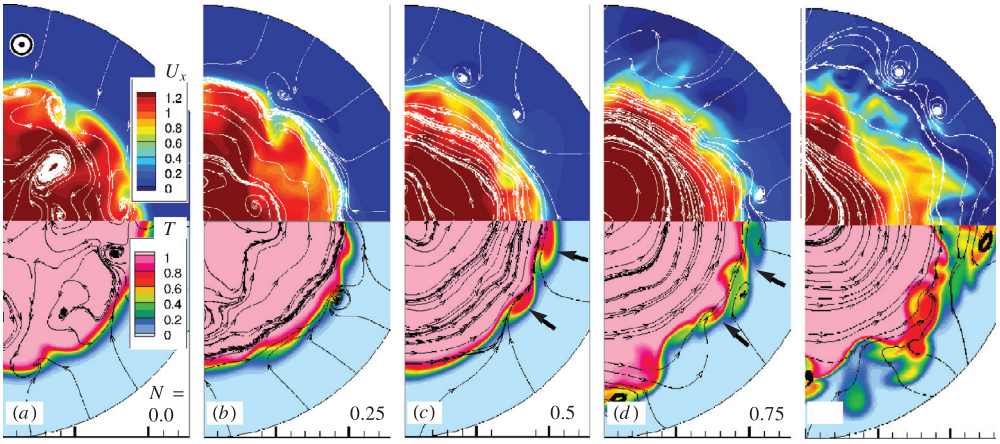

Fig. 7. Instantaneous axial velocity (top) and temperature (bottom) field together with streamlines in $r-\phi$ plane at $x/D = 0.5$ for various N.

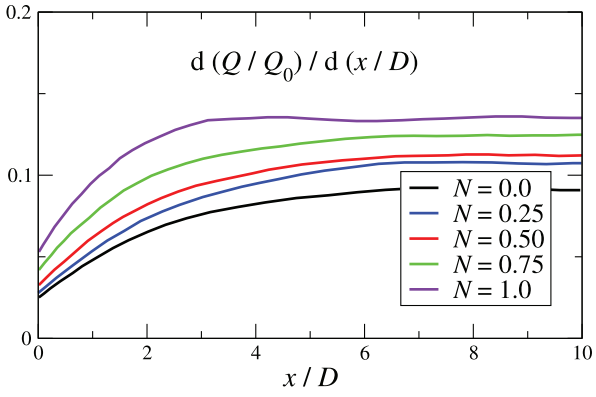

Fig. 8. The normalized entrainment against the downstream distance.

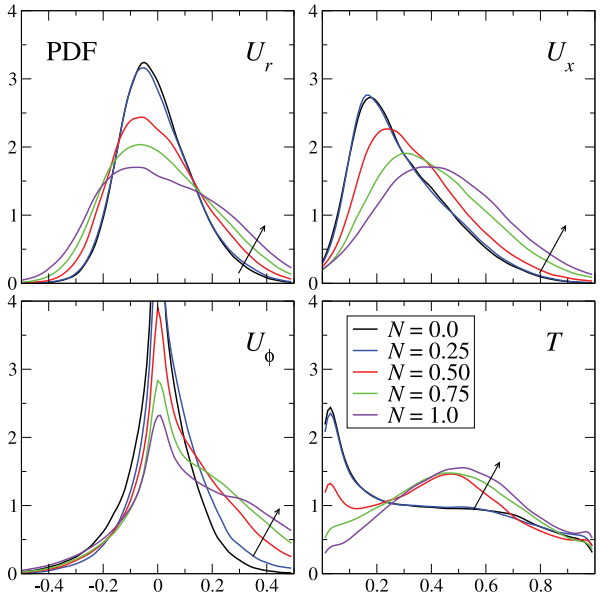

Fig. 9. PDF of all velocity components and temperature in the shear layer at $x/D = 1.0$, $r/D = 0.5$.

features with recognizable streaky structures, starting at $N = 0.5$ the entrainment is enhanced by the strong azimuthal shear layer. The helical waves (Liang and Maxworthy, 2005) are formed which are especially evident in the instantaneous temperature field (indicated by black arrows). The rotation is known to destabilize a wide range of high azimuthal wavenumbers under the influence of the centrifugal instability (Gallaire and Chomaz, 2004). According to the streamline patterns, these helical large-scale perturbations seem to be the main ingredient in the entrainment mechanism. Further increase in N makes the wavy high/low temperature "interface" more irregular indicating enhanced mixing. These patterns are preserved at very high rotation rates up to $N \approx 5.0$ as observed in the simulations of the rotating-pipe co-annular jet (Mullyadzhanov et al., 2015). To quantify the integral entrainment we followed the definition of Wygnanski and Fiedler (1969) and Crow and Champagne (1971) and calculated dQ/dx, where

$$Q(x) = 2\pi\rho \int_0^\infty \overline{U}_x(x,r) r dr$$

is the mass flux through the $r-\phi$ plane. The variation of dQ/dx normalized with $Q_0 = Q(x=0)$ and D is shown in Fig. 8. The results are consistent with previous knowledge. Close to the nozzle the entrainment enhanced by rotation rapidly grows and approaches the constant value in accord with to the self-similarity concept (Schlichting and Gersten, 2003).

Örlü and Alfredsson (2008) extensively discussed single and joint probability density distributions (PDFs) of the axial velocity and temperature in the region $4 \le x/D \le 6$ comparing jets at $N = 0.0$ and $N = 0.5$. We analyzed the near nozzle shear layer at $x/D = 1$ in order to compliment the previous studies and get more information on the entrainment mechanisms. Fig. 9 shows some single PDFs of all velocity components and temperature at different rotation rates. The tails of the radial velocity PDF notably increase with N indicating active 'in' and 'out' motion enhancing heat transfer/rate of mixing. While the distribution for U_x and U_ϕ shows an increase of the positive events with N, which is due to faster spreading rate and rotation, the PDF of T clearly demonstrates the peak at $T \approx 0.5$ starting from $N = 0.5$.

Fig. 10 shows the joint PDF of the radial and axial velocity with temperature. From this representation it is clear that for $N = 0.0$ the entrainment of 'cold' ambient fluid occurs at $U_r \approx -0.07$ and $U_x \approx 0.15$. With the increase in N some significant changes in the PDF landscape take place. Note that for both (U_r, T) and (U_x, T) there are three peaks although the amplitude varies with N. There is the same peak with negative U_r (or low U_x) and $T \approx 0.0$. For $N = 0.5$ this maximum is dominant as for $N = 0.0$ and, as mentioned above, corresponds to the entrainment events of the 'cold' fluid to the 'hot' jet core. The second peak has $U_r \approx 0.0$ (or $U_x \approx$

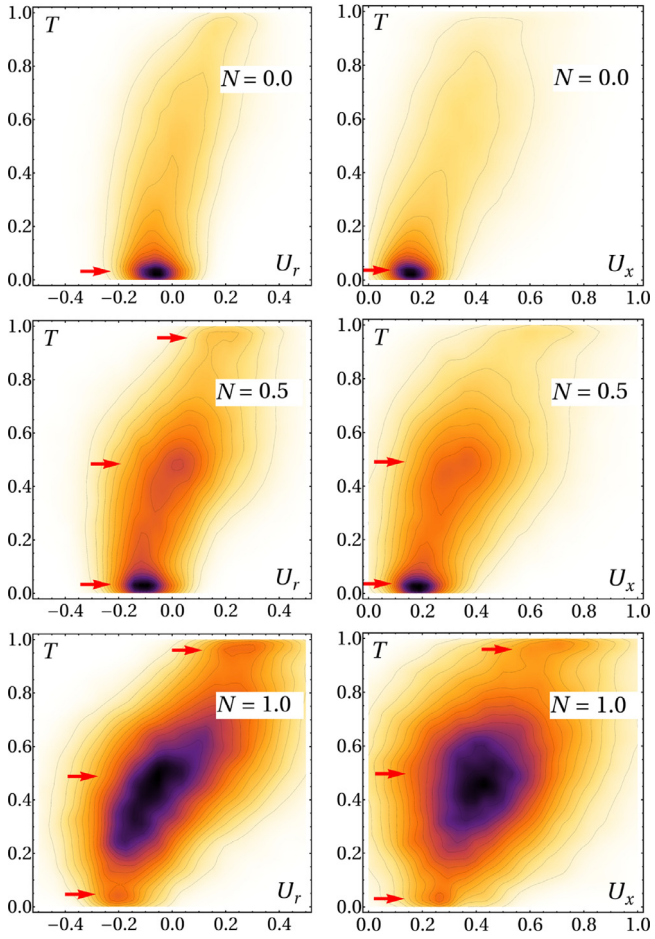

Fig. 10. Joint PDF of two pairs of variables, i.e. (U_r, T) and (U_x, T), in the shear layer at $x/D = 1.0$, $r/D = 0.5$. The color scheme ranges from the minimum (white) to maximum (black) value of the PDF.

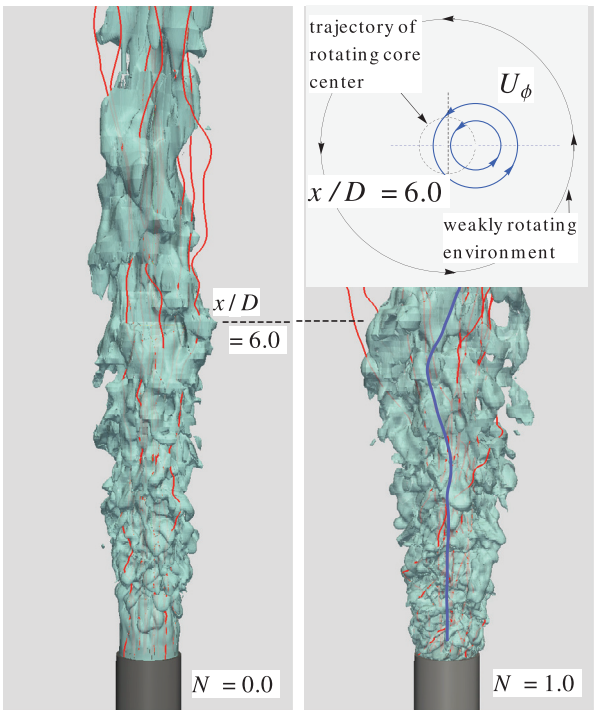

Fig. 11. Isosurface of $T = 0.4$ for $N = 0.0$ (left) and $N = 1.0$ (right). Red lines denote the instantaneous streamlines. A blue line (for $N = 1.0$) shows the core of the jet. The inset on the right shows the schematic explanation of the counter-rotating jet core phenomenon. (For interpretation of the references to colour in this figure legend, the reader is referred to the web version of this article.)

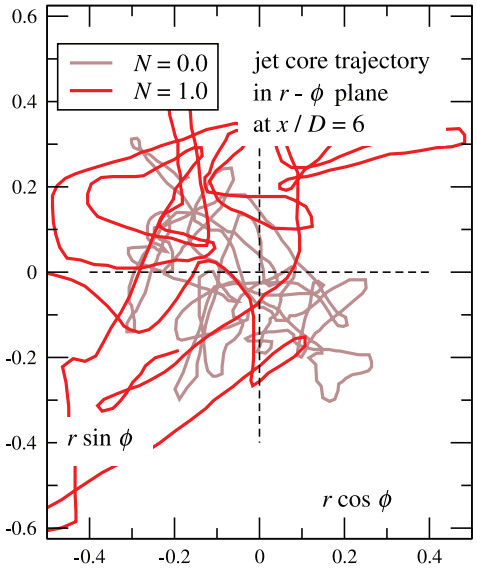

Fig. 12. The trajectory of the rotating core center evolution during $\Delta t = 10D/U_b$ at $x/D = 6$ in $r - \phi$ plane. The jet center is defined as the maximum of the axial velocity.

0.4) and $T \approx 0.5$ describing the presence of well-mixed fluid. The third, hardly recognizable peak, has $U_r \approx 0.2$ (or $U_x \approx 0.6$) and $T \approx 1.0$ corresponding to the events with 'hot' fluid from the core ejecting to the periphery. For $N = 1.0$ the dominant peak becomes the one describing well-mixed fluid with almost zero radial velocity. These arguments and observations are in line with the single PDFs discussed above.

The last issue we investigated in this paper is the phenomenon of the weakly counter-rotating jet core appearing at $x/D \approx 6.0$. Fig. 11 shows the isosurface of $T = 0.4$ for $N = 0.0$ and $N = 1.0$ together with streamlines. The visualization demonstrates the enhanced mixing properties of the swirling jet due to strong azimuthal shear close to the nozzle. Further downstream apparent large-scale deviations from the centerline of the jet core is evident for the rotating case at the position where negative $\overline{U}_\theta$ is observed (see Fig. 5). This unsteadiness is irregular and appears as the meandering and rotating motion of the jet core around the symmetry axis. To get more impression on this phenomenon the inset in Fig. 11 depicts a schematic of the fluid rotation at $x/D = 6.0$. Taking into account the distribution of the tangential velocity, the deviation of the jet core from the center leads to the appearance of the area with $U_\theta < 0$ close to $r = 0$. If these deviations are statistically significant, we obtain the effect in time-averaged fields, i.e. the region with $\overline{U}_\theta < 0$. The trajectory of the jet core center defined as the local maximum of the axial velocity at $x/D = 6$ is traced in Fig. 12 for non-swirling and swirling ($N = 1.0$) jets for some period of time. Note that the trajectory line is more dense for $N = 0.0$ due to the higher axial centreline velocity compared to swirling jets (see Fig. 4). It is also more compact compared to the swirling case due to the absence of centrifugal instability leading to the meandering motion of the jet core. The root-mean-square of the radial coordinate of the jet center is $\overline{r}/D \approx 0.19$ for $N = 0.0$ and $\overline{r}/D \approx 0.37$ for $N = 1.0$.

The observed meandering of the jet core suggests the application of the Fourier analysis with respect to the azimuthal angle ϕ. The LES snapshots of (U_r, U_x, U_ϕ) at some x position are

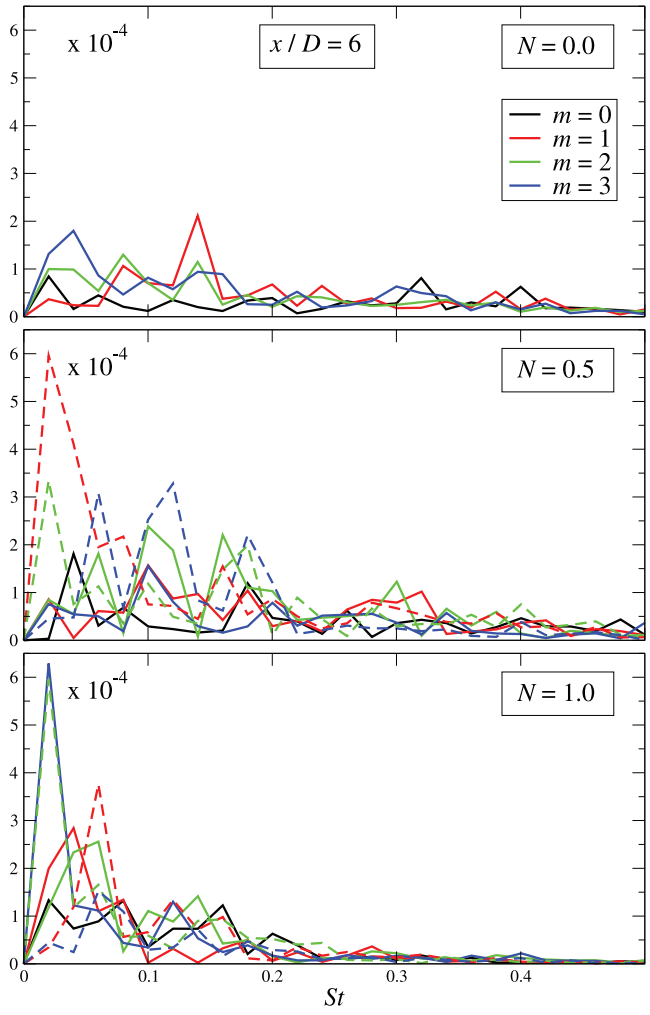

Fig. 13. The time power spectrum for low azimuthal modes at $x/D = 6.0$ and $r/D = 0.5$ for various N against the Strouhal number. Note that solid lines show $m \geq 0$ while dashed lines denote negative values.

decomposed into complex Fourier coefficients $U_i(r, m, f)$ yielding

$$U_i(r, m, f) = \frac{1}{2\pi t_{tot}} \int_0^{2\pi} \int_0^{t_{tot}} U_i(r, \phi, t) e^{im\phi - 2\pi i f t} d\phi dt,$$

where m is the integer azimuthal wavenumber. The squared modulus of the vector with components $U_i(r, m, f)$ shows the amount of turbulent kinetic energy in a single azimuthal mode. This value is presented in Fig. 13 against the Strouhal number $St = fD/U_b$ for various N. Co-rotating modes with $m > 0$ rotate with the mean flow while counter-rotating modes have $m < 0$. In general, the increase in N provides the increase of the turbulent kinetic energy for low m modes. While for $N = 0.0$ the level of fluctuations is quite low, $m = -1$, -2 and -3 become energetic for $N = 0.5$. Further increase in N adds on co-rotating modes in agreement with Oberleithner et al. (2012). The mode with $m = 3$ compensate $m = -2$ while $m = \pm 1$ have more or less equal level of energy. It should be noted that the considered position $x/D = 6$ features a low level of the turbulent kinetic energy and azimuthal velocity providing only low-frequency oscillations. However, the present wavenumber analysis quantitatively supports the above visualizations of the counter-rotating jet core due to meandering motion.

5. Conclusions

We performed Large-eddy simulation of a rotating-pipe jet at $Re = 5300$ and $N = 0 - 1$ to study the mixing characteristics and coherent structures in the near-nozzle area. The simulations aimed at providing a further insight into the near-field physics of moderately swirling jets and, in particular, at clarifying the entrainment mechanisms close to the nozzle and the phenomenon of counter-rotating jet core observed earlier experimentally by Facciolo and Alfredsson (2004) and others. The main findings are summarized as follows:

- The comparison of the time-averaged characteristics with the data from the literature showed very good agreement justifying our confidence that the flow and turbulence physics is simulated correctly.
- No large-scale coherent structures akin to the Kelvin–Helmholtz vortical rings common in the 'top-hat' jets were identified close to the nozzle. At low swirl rates ($N \leq 0.25$) the streaky structures supplied by the fully developed pipe flow can be traced for a length of $x/D \leq 1$. For higher rotations ($N \geq 0.75$) a strong azimuthal shear layer immediately destroys these structures.
- The consequence of the centrifugal instability, i.e. the events of entrainment of 'cold' fluid to the jet core and ejection of 'hot' fluid toward the periphery were observed in the instantaneous fields of the velocity and a passive scalar (temperature) and quantified using the single and joint probability density functions.
- In agreement with the previous research reported in the literature we observed a small counter-rotation region with $\overline{U}_\theta < 0$ close to the jet center at $x/D \approx 6$. The analysis of the instantaneous fields indicated that this phenomenon is due to the meandering and precessing of the jet core around the flow axis. The Fourier analysis with respect to the azimuthal direction and time reveals an interplay between the co- and counter-rotating modes.

The simulation results provide a verified comprehensive dataset that can serve for benchmarking other computational and experimental results.

Acknowledgement

This work is funded by Russian Science Foundation under the grant No. 14-29-00203. The computational resources are provided by Siberian Supercomputer Center SB RAS (Novosibirsk) and Joint Supercomputer Center RAS (Moscow). We thank R. Sandberg and R. Orlü for providing the DNS and experimental data and the referees for helpful comments and suggestions.

Appendix A. Validation of precursor simulations

To generate the inflow conditions we perform a separate precursor LES simulation of a flow through a $5D$ pipe with periodic boundary conditions at $Re = 5300$ and various N. The mesh provides a DNS-like resolution and consists of 2.8×10^6 cells, i.e. $80 \times 256 \times 128$ cells in radial, tangential and streamwise directions, respectively. The unstructured grid made of prisms is used for $r/D < 0.35$ while hexahedral cells are used closer to walls. The first grid point from the wall has $\Delta r/D = 0.00115$ providing that $r^+ < 1$. To validate the computations we use the available DNS data of Eggels et al. (1994), Wu and Moin (2008) for $N = 0$ and Orlandi and Fatica (1997), Ould-Rouiss et al. (2010) for $N = 0.5$ and $N = 1$. The comparison shows very good agreement for all cases, see Fig. A.14. A subsequent time series with $\Delta t = 2.5 \times 10^{-3} D/U_b$ of 20,000 slices at some $x =$ const of three instantaneous velocity components have

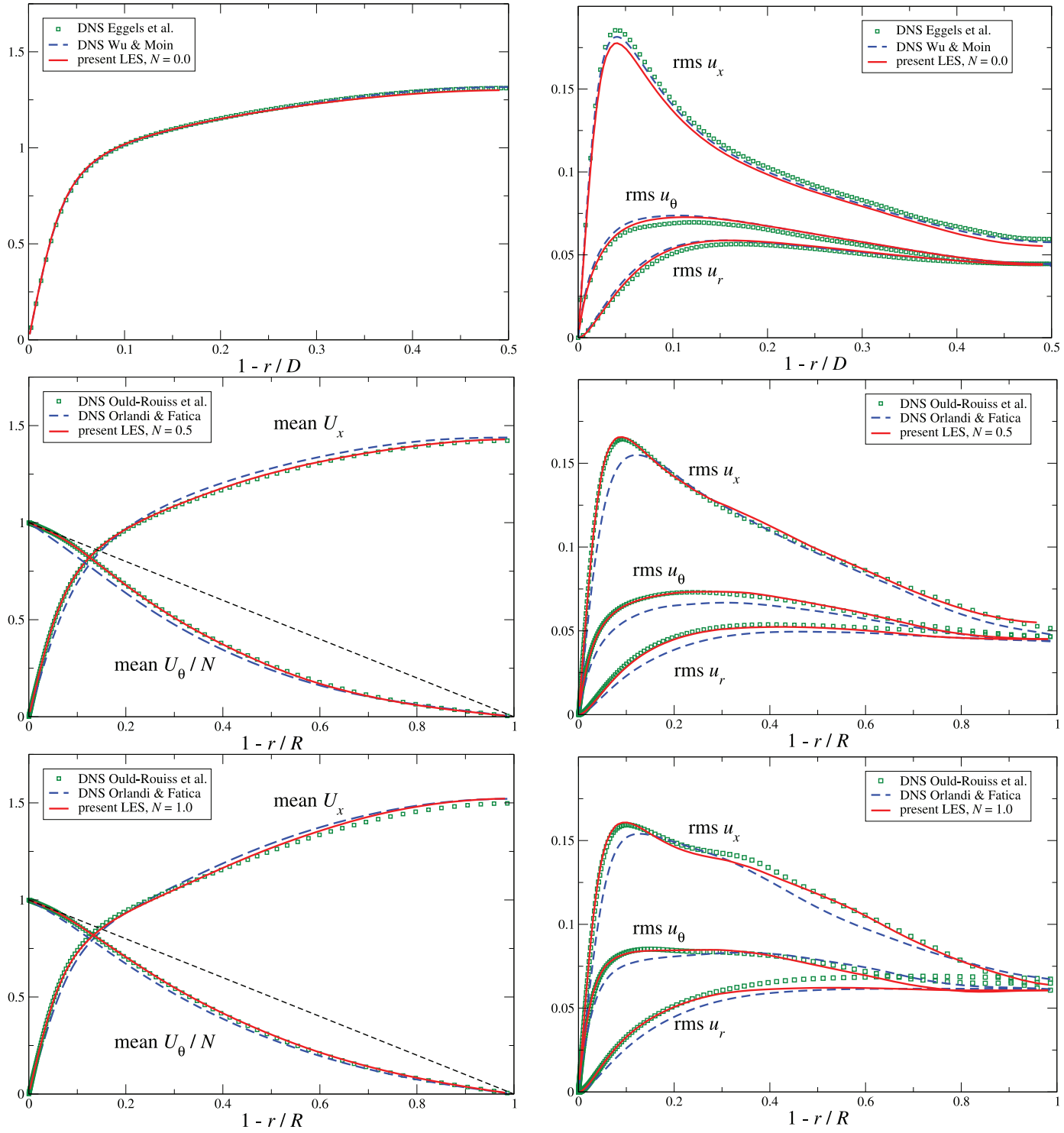

Fig. A14. Left: radial profiles of the mean axial and tangential velocity. Right: profiles of the normal stresses.

been recorded to disk and further used as the inflow conditions for the main jet computation for all N considered.

References

Alekseenko, S.V., Dulin, V.M., Kozorezov, Y.S., Markovich, D.M., 2008. Effect of axisymmetric forcing on the structure of a swirling turbulent jet. Int. J. Heat Fluid Flow 29, 1699–1715.

Ball, C.G., Fellouah, H., Pollard, A., 2012. The flow field in turbulent round free jets. Prog. Aerosp. Sci. 50, 1–26.

Billant, P., Chomaz, J., Huerre, P., 1998. Experimental study of vortex breakdown in swirling jets. J. Fluid Mech. 376, 183–219.

Capone, A., Soldati, A., Romano, G.P., 2013. Mixing and entrainment in the near field of turbulent round jets. Exp. Fluids 54 (1), 1–14.

Crow, S., Champagne, F., 1971. Orderly structure in jet turbulence. J. Fluid Mech. 48 (3), 547–591.

Eggels, J.G., Unger, F., Weiss, M.H., Westerweel, J., Adrian, R.J., Friedreich, F., Nieuwstadt, F.T.M., 1994. Fully developed turbulent pipe flow: a comparison between direct numerical simulation and experiment. J. Fluid. Mech. 268, 175–209.

Facciolo, L., Alfredsson, P.H., 2004. The counter-rotating core of a swirling turbulent jet issuing from a rotating pipe flow. Phys. Fluids 16, L71–L73.

Facciolo, L., Tillmark, N., Talamelli, A., Alfredsson, P.H., 2007. A study of swirling turbulent pipe and jet flows. Phys. Fluids 19, 035105.
Gallaire, F., Chomaz, J.-M., 2004. Mode selection in swirling jet experiments: a linear stability analysis. J. Fluid Mech. 494, 223–253.
Germano, M., Piomelli, U., Moin, P., Cabot, W.H., 1991. A dynamic subgrid-scale eddy viscosity model. Phys. Fluids A 3 (7), 1760–1765.
Leclaire, B., Jacquin, L., 2012. On the generation of swirling jets: high-Reynolds-number rotating flow in a pipe with a final contraction. J. Fluid Mech. 692, 78–111.
Liang, H., Maxworthy, T., 2005. An experimental investigation of swirling jets. J. Fluid Mech. 525, 115–159.
Loitsianskii, L.G., 1953. Propagation of a shirling jet in an infinite space filled with the same fluid. Prikl. Mat. Mech. 17 (3), 7.
Lucca-Negro, O., O'Doherty, T., 2001. Vortex breakdown: a review. Prog. Energy Combust. Sci. 27 (4), 431–481.
Luginsland, T., 2015. How the nozzle geometry impacts vortex breakdown in compressible swirling-jet flows. AIAA J 53 (10), 2936–2950.
Luginsland, T., Gallaire, F., Kleiser, L., 2016. Impact of rotating and fixed nozzles on vortex breakdown in compressible swirling jet flows. Eur. J. Mech. B/Fluids 57, 214–230.
Luginsland, T., Kleiser, L., 2015. Effects of boundary conditions on vortex breakdown in compressible swirling jet flow simulations. Comput. Fluids 109, 72–84.
Maciel, Y., Facciolo, L., Duwig, C., Fuchs, L., Alfredsson, P., 2008. Near-field dynamics of a turbulent round jet with moderate swirl. Int. J. Heat Fluid Flow 29, 675–686.
McIlwain, S., Pollard, A., 2002. Large eddy simulation of the effects of mild swirl on the near field of a round free jet. Phys. Fluids 14, 653.
Mehta, R.D., Wood, D.H., Clausen, P.D., 1991. Some effects of swirl on turbulent mixing layer development. Phys. Fluids A 3, 2716.
Miranda-Barea, A., Martinez-Arias, B., Parras, L., Burgos, M.A., del Pino, C., 2015. Experimental study of rotating Hagen-Poiseuille flow discharging into a 1:8 sudden expansion. Phys. Fluids 27, 034104.
Mullyadzhanov, R., Hadžiabdić, M., Hanjalić, K., 2015. LES investigation of the hysteresis regime in the cold model of a rotating-pipe swirl burner. Flow Turbul. Combust. 94 (1), 175–198.
Mullyadzhanov, R.I., Yavorskii, N.I., 2013. Solution of the problem of flow of a non-axisymmetric swirling submerged jet. J. Appl. Mech. Tech. Phys. 54 (2), 207–211.
Ničeno, B., Hanjalić, K., 2005. Unstructured large-eddy-and conjugate heat transfer simulations of wall-bounded flows. In: Faghri, M., Sunden, B. (Eds.), Modeling and Simulation of Turbulent Heat Transfer (Developments in Heat Transfer). WIT, UK.
Oberleithner, K., Paschereit, C., Seele, R., Wygnanski, I., 2012. Formation of turbulent vortex breakdown: intermittency, criticality, and global instability. AIAA J. 50 (7), 1437–1452.
Oljaca, M., Gu, X., Glezer, A., Baffico, M., Lund, F., 1998. Ultrasound scattering by a swirling jet. Phys. Fluids 10 (4), 886–898.
Orlandi, P., Fatica, M., 1997. Direct simulations of turbulent flow in a pipe rotating about its axis. J. Fluid Mech. 343, 43–72.
Örlü, R., 2009. Experimental Studies in Jet Flows and Zero Pressure-Gradient Turbulent Boundary Layers Ph.D. thesis. KTH, Stockholm, Sweden.
Örlü, R., Alfredsson, P.H., 2008. An experimental study of the near-field mixing characteristics of a swirling jet. Flow Turbul. Combust. 80, 323–350.
Ould-Rouiss, M., Dries, A., Mazouz, A., 2010. Numerical predictions of turbulent heat transfer for air flow in rotating pipe. Int. J. Heat Fluid Flow 31, 507–517.
Panda, J., McLaughlin, D.K., 1994. Experiments on the instabilities of a swirling jet. Phys. Fluids 6 (1), 263.
Pratte, B.D., Keffer, J.F., 1972. The swirling turbulent jet. J. Basic Eng. 94 (4), 739–747.
Rose, W.G., 1962. A swirling round turbulent jet: 1 – mean-flow measurements. J. Appl. Mech. 29 (4), 615–625.
Sandberg, R.D., Sandham, N.D., Suponitsky, V., 2012. DNS of compressible pipe flow exiting into a coflow. Int. J. Heat Fluid Flow 35, 33–44.
Sanmiguel-Rojas, E., Burgos, M.A., del Pino, C., Fernandez-Feria, R., 2008. Three-dimensional structure of confined swirling jets at moderately large reynolds numbers. Phys. Fluids 20, 044104.
Schlichting, H., Gersten, K., 2003. Boundary-Layer Theory. Springer Science & Business Media.
Wu, X., Moin, P., 2008. A direct numerical simulation study on the mean velocity characteristics in turbulent pipe flow. J. Fluid. Mech. 608, 81–112.
Wygnanski, I., Fiedler, H., 1969. Some measurements in the self-preserving jet. J. Fluid Mech. 38 (3), 577–612.